Editors' Suggestion | Featured in Physics

Amplification of Acoustic Forces Using Microbubble Arrays Enables Manipulation of Centimeter-Scale Objects

Rahul Goyal,[1] Athanasios G. Athanassiadis,[1,*] Zhichao Ma,[1,†] and Peer Fischer[1,2]
[1]Max Planck Institute for Intelligent Systems, Heisenbergstr. 3, 70569 Stuttgart, Germany
[2]Institute of Physical Chemistry, University of Stuttgart, Pfaffenwaldring 55, 70569 Stuttgart, Germany

(Received 28 December 2021; revised 18 April 2022; accepted 13 May 2022; published 24 June 2022)

Manipulation of macroscale objects by sound is fundamentally limited by the wavelength and object size. Resonant subwavelength scatterers such as bubbles can decouple these requirements, but typically the forces are weak. Here we show that patterning bubbles into arrays leads to geometric amplification of the scattering forces, enabling the precise assembly and manipulation of cm-scale objects. We rotate a 1 cm object continuously or position it with 15 μm accuracy, using sound with a 50 cm wavelength. The results are described well by a theoretical model. Our results lay the foundation for using secondary Bjerknes forces in the controlled organization and manipulation of macroscale structures.

DOI: 10.1103/PhysRevLett.128.254502

Directed assembly and manipulation of objects in fluids is of fundamental interest and finds applications in advanced manufacturing [1,2], and robotics [3–5]. The most prominent approaches for directed assembly use fluidic effects [6,7], magnetic [8,9] and electric fields [10–12], and to a lesser degree optical fields [13–15]. More recently, acoustic fields have emerged as a promising approach, as they can propagate through most media, generally do not require special responsive materials, can be used to manipulate biological cells, and offer the possibility of dynamic control [16–21].

The majority of work in acoustic assembly is based on the primary radiation force that is directly exerted on objects and particles by the acoustic field [22–24]. Differences in sound speed and density between the object and the surrounding environment cause scattering, which produces an acoustic radiation force on the object [25]. Particles, including cells, can be assembled at the nodes or antinodes of an acoustic field. Additionally, acoustic streaming flows can exert forces [26] that can be used to manipulate and assemble micro-objects in solution [18,27–29].

However, existing acoustic assembly techniques are generally restricted by the wavelength of sound. Objects manipulated by the field must be smaller than a wavelength, while the positioning accuracy is set by the field shape, which cannot have features much smaller than a wavelength. On top of this, higher attenuation at high frequencies makes long-wavelength sound preferable. These factors introduce a trade-off for large objects or structures: high-frequency fields are necessary for precise positioning, but are less effective for larger length scales.

We present an alternative approach for the accurate assembly of macrostructures, based on secondary acoustic radiation force between resonant scatterers in a sound field. Microbubbles are well-known resonant objects, scattering sound efficiently at long wavelengths compared to the bubble size. The secondary radiation forces between bubbles arise from coupling between scattered fields, and are known as secondary Bjerknes forces [30]. Such forces have been used to manipulate individual bubbles [31] and can explain the clustering dynamics of bubble clouds [32–35]. Since they generally fall in the range of 10 nN, such forces are considered too weak for applications in larger systems. Here, we show how secondary radiation forces between $\sim$100 μm bubbles can be amplified, enabling acoustic assembly and manipulation of cm-scale structures (Fig. 1), while using acoustic wavelengths that are much larger than the objects and the bubbles.

The secondary Bjerknes force on a bubble with radius R_0 at the origin, from an identical bubble at position $\vec{r}$, is given by [36]

$$\vec{F}_B = 2\pi\rho R_0^4 \omega^2 \delta^2 \vec{r}/r^3. \quad (1)$$

where, ρ is the density of the liquid, $\omega = 2\pi f$ is the radial oscillation frequency, and δ is the radial oscillation amplitude of each bubble. We assume that the bubble sizes R_0 and separation r are both much smaller than the acoustic wavelength λ. The force between the bubbles is central (along $\vec{r}$) and attractive, as shown in Fig. 1(a). For bubbles

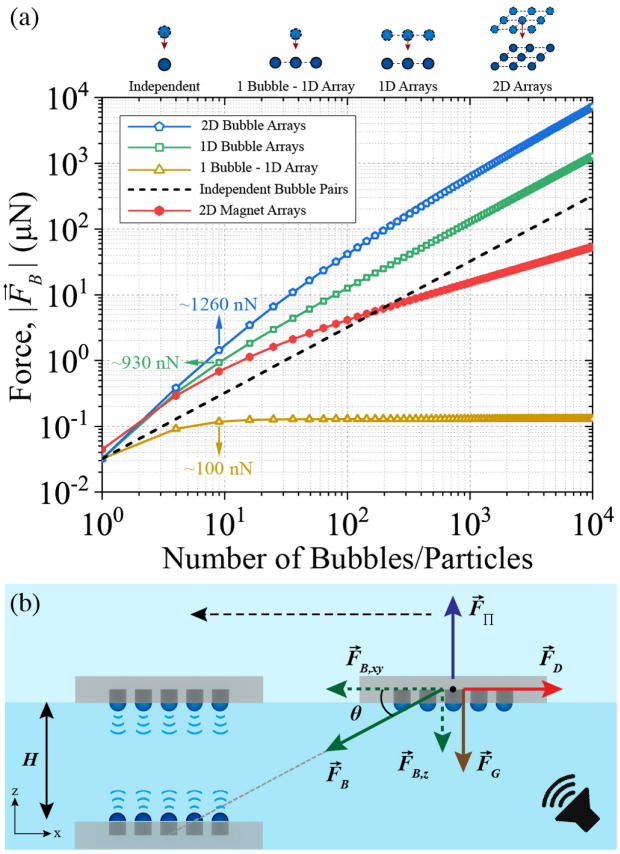

FIG. 1. Patterning bubbles amplifies their interactions. (a) Force scaling for bubble arrays as a function of array size in different geometries. The geometries are drawn schematically above. Interactions between two arrays (blue pentagons) amplify the forces by up to a factor 25 compared to an equivalent number of independent bubbles (black dashed line). Bubble arrays also generate larger forces than comparable magnetic arrays (red hexagons). (b) Forces acting between two structures with embedded bubble arrays in a sound field. The floating structure moves due to the lateral component of the secondary Bjerknes force $\vec{F}_{B,xy}$. The motion is resisted by fluid drag $\vec{F}_D$. Buoyancy $\vec{F}_\Pi$ balances gravity $\vec{F}_G$ and the vertical component of the Bjerknes forces $\vec{F}_{B,z}$.

of radius $R_0 = 150$ μm separated by $r = 1$ mm in water, with $\delta = 5$ μm and $f = 3.3$ kHz, the attractive force is $F_B = 28$ nN.

To scale up these forces we pattern microbubbles into an array, which geometrically amplifies the secondary Bjerknes force, as shown in Fig. 1(a). We first consider the force on a single bubble from an array of bubbles with spacing $\Delta = 500$ μm. The force between the array and the bubble is calculated by summing $\vec{F}_B$ between the free bubble and each bubble in the array (indexed by i): $\vec{F}_{B1} = \sum_i \vec{F}_B(\vec{r}_i)$. Bubbles in the array are assumed to be rigidly fixed in place, so that their interaction does not lead to rearrangement of the array. Moreover, because of the high acoustic contrast between water and air, and the relatively weak contrast between water and PDMS, scattering from the PDMS structure would be significantly weaker than the bubble scattering and is thus ignored. As shown in Fig. 1(a), the force between one bubble and a line of 9 bubbles increases to ~100 nN [Fig. 1(a), yellow arrow], but then does not increase as more bubbles are added, due to the r^{-2} dependence of the secondary Bjerknes force. If however, two arrays of bubbles interact, each bubble in one array will always have a nearby partner in the other, leading to a growth of F_B with the number of bubbles in each array. For two 9-bubble arrays separated by a height $H = 1$ mm, the attractive force jumps to 930 nN (green arrow) [37]. The force amplification is even more dramatic when considering 2D arrays of bubbles: the secondary Bjerknes force between two 3×3 arrays of bubbles is 1260 nN (blue arrow).

As the number of bubbles N in each array increases, so does the force amplification. However, the force does not grow linearly with N, as would be the case for N independent pairs of bubbles (black-dashed line). Instead, the force between bubble arrays grows superlinearly with N. As shown in Fig. 1(a), the force between arrays scales as approximately $F \sim N^{1.6}$ for low N, transitioning to an asymptotic scaling $F \sim N$ for large N. The superlinear scaling thus points to the importance of long-range interactions between bubbles in the arrays, which are absent when calculating the force based on independent bubble pairs. For our selected parameters, the long-range coupling in the arrays gives rise to a maximum amplification of ≈25× over the force produced by independent bubble pairs for very large N. However, extremely large arrays are not necessary for meaningful amplification. A 2D array with $N = 100$ already provides a factor 13 amplification over N independent bubble pairs, generating nearly 0.1 mN of force.

The bubble arrays also scale to large forces more effectively than magnetic systems that are popular in assembly applications. Although magnetic forces are typically considered to be much stronger than acoustic forces between bubbles, we find these benefits are limited to small system dimensions. We calculate the magnetic forces between two arrays of paramagnetic iron (II) oxide particles with an equivalent geometry to the bubble arrays discussed above, and a dipole strength of 2.72×10^{-7} Am^2 [37]. As shown in Fig. 1(a), although the force between two magnetic particles is larger than that between two bubbles, the force between bubble arrays scales more rapidly with N, and generates larger forces for $N > 1$. The advantages of the bubble arrays are most notable at large range. For close-range interactions (separations on the order of the particle size), the magnetic arrays produce higher forces [37]. We attribute the favorable force scaling for bubbles to the longer-range interactions between bubbles in the array, which scale as r^{-2}, as opposed to r^{-4} for magnetic dipoles.

To experimentally demonstrate manipulation with the secondary Bjerknes forces, we embed bubble arrays into

~1 cm-diameter PDMS structures using soft lithography [49]. An array of 11×11 cylindrical cavities is molded into the center of each structure. Each cavity has a diameter $2R_0 = 300$ μm and height $L = 275$ μm. The cavities are uniformly spaced with a pitch $\Delta = 500$ μm. The cavities are only open on one face of the disk, so that when the PDMS structures are placed in a reservoir of water [Fig. 1(b)], air bubbles are trapped. In the presence of an acoustic field, the bubble surfaces vibrate, with a primary resonance (maximum vibration amplitude) at 3.3 kHz (see movie S1 [37]). Because of the long acoustic wavelength in water (450 mm), all bubbles in the system are excited in phase, which lowers the resonance compared to predictions for a single bubble interface [37].

We fix the lower structure to the bottom of the reservoir while the upper structure floats freely on the air-water interface, with a vertical distance H separating the bubble arrays. A detailed description of the experiments is provided in the Supplemental Material [37]. When the acoustic transducer attached to the reservoir is driven at the bubble resonance, the attractive secondary Bjerknes interaction between the bubbles drives motion of the free structure. The horizontal component of the acoustic forces between the structures causes the free structure to move along the water surface, while the vertical component is balanced by buoyancy. Other forces acting on the structure include fluid drag and gravity, as shown in Fig. 1(b).

The acoustic forces on the bubble arrays are large enough to drive assembly of cm-scale PDMS structures, as depicted in Fig. 2(a). For static assembly of two structures relative to each other, we leverage the full 11×11 bubble arrays as shown in Fig. 2(a). Experimental images of the alignment process are shown in Fig. 2(b) for a water layer of height $H = 1$ mm. The complete response of the array can be seen in movie S2 [37]. Time-lapse photographs reveal the mobile array moving towards a stable trap position at 10 to 30 mm/s until it is aligned above the fixed bubble array [red square in Fig. 2(b)]. Repeating the same experiments under a microscope with a 10× objective (see movie S3 [37]), we measure an alignment accuracy of 14 μm $\pm$ 4 μm for the cm-sized structures, which corresponds to an accuracy of 0.1% relative to the size of objects, and 0.003% relative to the acoustic wavelength.

We performed two further experiments to confirm the dominant role of secondary Bjerknes forces in our system. First, we repeated the alignment experiments with the mobile structure replaced by a bubble-free PDMS slab. Second, we repeated the experiment with the original floating structure but without the fixed alignment target. In both experiments, the floating structure did not respond when the transducer was turned on, indicating that assembly is not driven by forces or streaming effects from the primary acoustic field. Instead, assembly must be driven by the secondary Bjerknes forces between the bubble arrays.

We further validate the role of secondary Bjerknes forces using a numerical model of the structure's dynamics. During assembly, the bubble-embedded structure undergoes damped oscillatory motion as it aligns with the fixed alignment target (see movie S2 [37]). The dynamics reveal that the attractive force drives the motion, while viscous drag at the water interface damps it. Because of the length and velocity scales, inertia remains relevant. The assembly dynamics can therefore be described by the differential equation

$$m\frac{\partial^2 \vec{x}}{\partial t^2} = \vec{F}_{B2}(\vec{x}) - \beta\frac{\partial \vec{x}}{\partial t}, \tag{2}$$

where $\vec{x}$ denotes the center of mass of the free PDMS structure relative to the stationary structure, m denotes the mass of the structure, and $\beta \approx 2.5 \times 10^{-4}$ N s m^{-1} is a viscous damping coefficient that is found from experiments [37]. $\vec{F}_{B2}(\vec{x})$ is the spatially dependent force on the mobile array from the fixed one.

The force between the arrays is calculated by summing the pairwise Bjerknes force [Eq. (1)] between the bubbles in the two arrays: $\vec{F}_{B2}(\vec{x}) = \sum_{i=1}^{N}\sum_{j=1}^{N}\vec{F}_B(\vec{r}_{ij})$ [37]. Here,

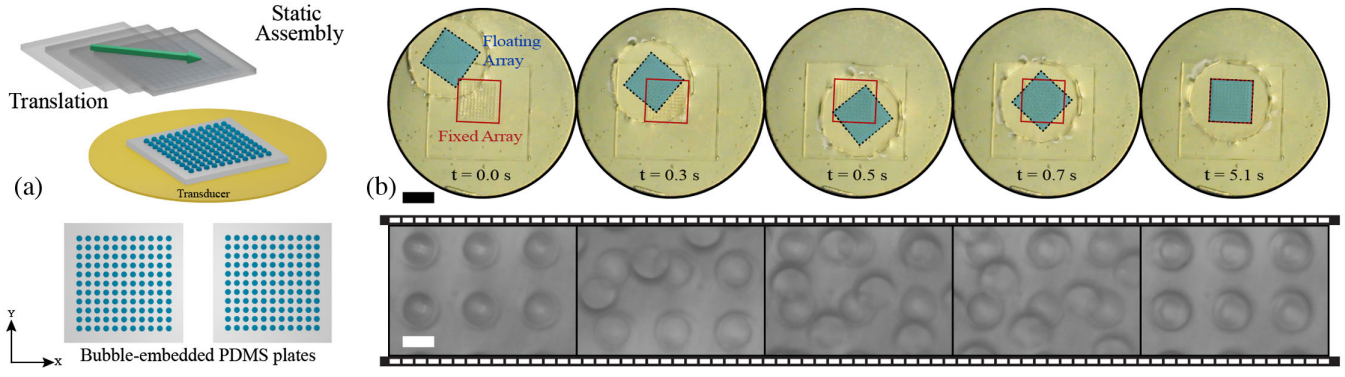

FIG. 2. Assembly and alignment of sound-activated structures. (a) Schematic of the assembly experiment. (b) Experimental images following the alignment of the floating array (blue square) to the fixed array (red square) for $H = 1$ mm. The microscope images below show the central region of the fixed array, demonstrating precise alignment. Scale bars: 5 mm (black) and 300 μm (white).

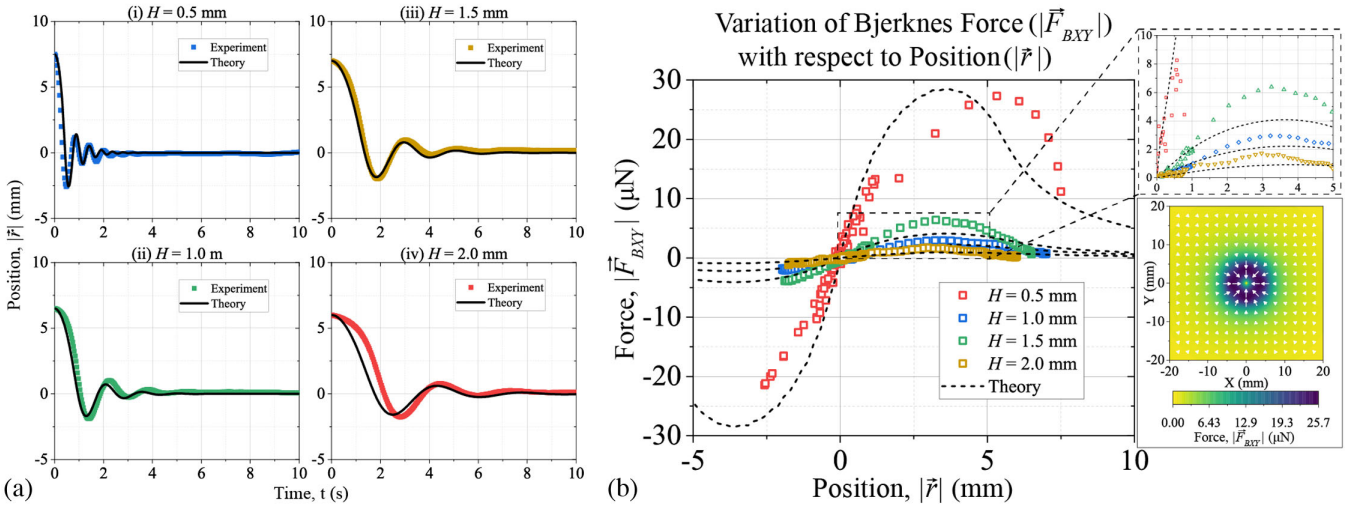

FIG. 3. Comparison of numerical model to experiments. (a) Simulated motion of the floating array under the influence of secondary Bjerknes forces (black lines) for four different water heights H. The simulation results match experimental measurements very well (colored points). (b) The lateral force between the two bubble arrays also matches very closely between experiments (symbols) and the analytical prediction (dashed lines) [37]. Upper inset: zoomed region around $r = 0$ showing lower forces. Lower inset: 2D lateral force distribution showing a central, attractive trap.

$\vec{r}_{ij}$ denotes the displacement vector from bubble i in the free array and bubble j in the static array, which implicitly depends on the free array's position $\vec{x}$. The sums are taken over all N bubbles in each array. The horizontal component of the force between the two arrays is always attractive and exhibits a ring-shaped maximum, as shown in Fig. 3(b) (inset). As described in Eq. (1), $\vec{F}_B$ depends on the pulsation amplitude δ of bubbles in the acoustic field. We estimate $\delta \approx 5$ μm based on optical measurements of the bubble oscillations (described in Supplemental Material [37]), which are consistent with other observations of excited bubbles in the literature [16]. Given the force field $\vec{F}_{B2}(\vec{x})$ and the measured parameters m and β, we can use Eq. (2) to estimate the dynamics of the free-floating structure due to the secondary Bjerknes forces between the arrays.

We compare the performance of our model to assembly experiments for multiple water gaps H between 0.5 and 2.0 mm. The measured positions of the mobile structure are compared to the simulated motion in Fig. 3(a). As described in the Supplemental Material [37], the model's free parameters δ and β demonstrate a weak dependence on H, which we attribute to fluidic interactions between the two plates that we do not model in this Letter. Nonetheless, the theoretically predicted trajectories are in excellent agreement with experiments. Both show that the assembly time increases for larger separations H. The model also accurately captures the measured overshoot and damped oscillation of the target as the mobile structure reaches its equilibrium position (see Movie S2 [37]). As an additional verification, we use the measured trajectories $\vec{x}(t)$ and Eq. (2) to estimate the spatially dependent secondary Bjerknes force acting on the mobile structure. As shown in Fig. 3(b), these estimates agree very well with the analytically calculated forces, in both trend and magnitude, revealing peak lateral attractive forces between 1 and 30 μN for different H. The inset in Fig. 3(b) shows the two-dimensional force on the floating array as a function of position [37]. The success of this simplified model to match the dynamics and force magnitude of the structures in experiments, accounting only for secondary Bjerknes forces between the arrays, demonstrates that the assembly process is dominated by these forces and not other effects such as streaming (see Movie S4 [37]). The analytical description can be used to then predict how the forces will scale with other parameters, such as the bubble radius. For example, when scaling the system up proportionally, it can be shown that the force will grow as $F_{B2} \sim R_0$, with larger bubbles generating larger forces [37]. This scaling should be valid until nonlinear effects or capillary forces lead to bubble breakup during oscillations.

Finally, we demonstrate that an asymmetric arrangement of bubbles in the two arrays can drive the continuous rotational motion of the structure, while simultaneously producing a central trap to maintain alignment. The torque arises from the in-plane Bjerknes forces acting on different bubbles within the freely rotating array. We create asymmetric bubble patterns by selectively blocking bubbles on the array as shown in Fig. 4(a). The analytically calculated force between the asymmetric bubble arrays is plotted in Fig. 4(b) [37]. The different patterns on the two structures skew the force distribution, generating a torque that varies with angle. However, there is no preferred direction to this motor, as in an electric motor. Instead the rotation direction is determined by the initial position and angular momentum

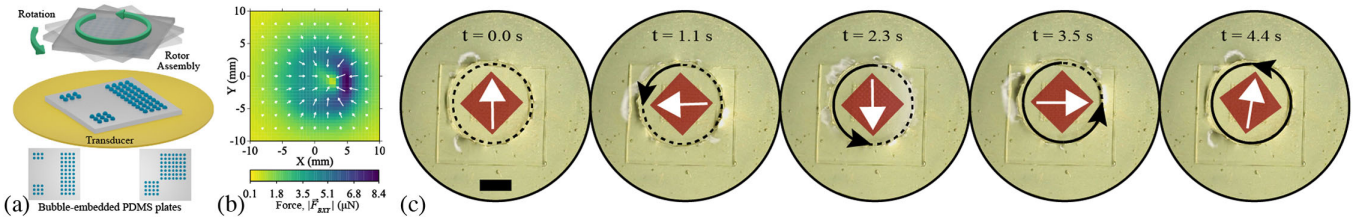

FIG. 4. Acoustic rotation of structures. (a) Schematic of asymmetric bubble arrays that lead to rotation of the free structure. (b) 2D distribution of the lateral secondary Bjerknes force between the structures shows a central trap that holds the mobile structure in place above the fixed one. (c) Experimental images of acoustically driven rotation of structure. Red colored rectangle and white colored arrow indicate the instantaneous position and orientation of the mobile structure, respectively. Scale bar: 5 mm. Images taken from Movie S5 [37].

of the rotor. Once it rotates in a specific direction, inertia maintains the rotation direction. The results of rotation experiments are shown in Fig. 4(c) and Movie S5 [37] for a $H = 1$ mm water gap. With the given parameters, our acoustic rotor spins at a rate of 1.4 rad s^{-1}, or about 14 RPM. By further designing different bubble patterns into fixed and mobile structures, it is expected that more complex manipulations could be realized.

In conclusion, we have introduced a method for directed assembly in liquids based on the secondary Bjerknes force between arrays of microbubbles. By using subwavelength bubbles, we eliminate the coupling between assembly precision, the acoustic wavelength, and the object size. Although scattering forces between bubbles are typically considered to be weak, arrays of bubbles can amplify their interactions by up to 25× compared to an equivalent number of individual bubble pairs. The benefits of bubble arrays arise from long-range interactions associated with the Bjerknes force, which leads to higher forces in macroscale systems, compared to comparable magnetic assembly. The μN-scale forces generated by an 11×11 array were used to rotate and translate cm-scale structures in solution. The assemblies form within seconds of the application of an external sound field, and persist as long as the sound field is applied, indicating the switchable nature of the proposed technique. Theoretical predictions of the forces and the motion dynamics agree well with experiments. We expect that the technique can be scaled to larger and heavier systems, albeit with slower dynamics because of increased drag. Size limitations should be set by the floating structure's weight and buoyancy.

This acoustic technique has the potential to facilitate directed assembly selectively and in a pre-programmed manner. While the demonstrations here have centered on larger cm-scale structures, scaling down the bubble and array dimensions should also permit the assembly of mm-scale and μm-scale structures. The all-acoustical strategy using bubble arrays to manipulate and assemble macrostructures could be combined with position-sensitive optical observations for contactless manipulation and control, and paves the way for potential applications in manufacturing, soft robotics and microfluidics.

This work was supported by the European Research Council under the ERC Advanced Grant Agreement HOLOMAN (No. 788296). Z. M. acknowledges support from the Alexander von Humboldt Foundation. R. G. acknowledges support from International Max Planck Research School for Intelligent Systems (IMPRS-IS). Z. M. proposed the work; R. G., A. G. A., and Z. M. designed the experiments; R. G. and A. G. A. developed the theoretical model; R. G. performed the experiments; R. G. and A. G. A. analyzed the data; A. G. A., Z. M., and P. F. supervised the work.

*thanasi@is.mpg.de
†zma@is.mpg.de

[1] M. Mastrangeli, S. Abbasi, C. Varel, C. Van Hoof, J.-P. Celis, and K. F. Böhringer, Self-assembly from milli- to nanoscales: Methods and applications, J. Micromech. Microeng. **19**, 083001 (2009).
[2] H. O. Jacobs, Fabrication of a cylindrical display by patterned assembly, Science **296**, 323 (2002).
[3] R. Gro, M. Bonani, F. Mondada, and M. Dorigo, Autonomous self-assembly in swarm-bots, IEEE Trans. Rob. **22**, 1115 (2006).
[4] M. Wehner, R. L. Truby, D. J. Fitzgerald, B. Mosadegh, G. M. Whitesides, J. A. Lewis, and R. J. Wood, An integrated design and fabrication strategy for entirely soft, autonomous robots, Nature (London) **536**, 451 (2016).
[5] S. Li, R. Batra, D. Brown, H.-D. Chang, N. Ranganathan, C. Hoberman, D. Rus, and H. Lipson, Particle robotics based on statistical mechanics of loosely coupled components, Nature (London) **567**, 361 (2019).
[6] V. Flauraud, M. Mastrangeli, G. D. Bernasconi, J. Butet, D. T. L. Alexander, E. Shahrabi, O. J. F. Martin, and J. Brugger, Nanoscale topographical control of capillary assembly of nanoparticles, Nat. Nanotechnol. **12**, 73 (2017).
[7] A. Barbot, H. Tan, M. Power, F. Seichepine, and G.-Z. Yang, Floating magnetic microrobots for fiber functionalization, Sci. Rob. **4**, eaax8336 (2019).
[8] R. M. Erb, H. S. Son, B. Samanta, V. M. Rotello, and B. B. Yellen, Magnetic assembly of colloidal superstructures with multipole symmetry, Nature (London) **457**, 999 (2009).

[9] K. A. Mirica, F. Ilievski, A. K. Ellerbee, S. S. Shevkoplyas, and G. M. Whitesides, Using magnetic levitation for three dimensional self-assembly, Adv. Mater. **23**, 4134 (2011).
[10] K.-F. Bohringer, K. Goldberg, M. Cohn, R. Howe, and A. Pisano, Parallel microassembly with electrostatic force fields, in *Proceedings of the 1998 IEEE International Conference on Robotics and Automation (Cat. No. 98CH36146)* (IEEE, Leuven, 1998), Vol. 2, pp. 1204–1211, 10.1109/ROBOT.1998.677259.
[11] F. Krisnadi, L. L. Nguyen, Ankit, J. Ma, M. R. Kulkarni, N. Mathews, and M. D. Dickey, Directed assembly of liquid metal-elastomer conductors for stretchable and self healing electronics, Adv. Mater. **32**, 2001642 (2020).
[12] D. Morales, L. Teulon, E. Palleau, T. Alnasser, and L. Ressier, Single-step binary electrostatic directed assembly of active nanogels for smart concentration-dependent encryption, Langmuir **34**, 1557 (2018).
[13] K. Dholakia, B. W. Drinkwater, and M. Ritsch-Marte, Comparing acoustic and optical forces for biomedical research, Nat. Rev. Phys. **2**, 480 (2020).
[14] L. Ouyang, J. P. K. Armstrong, M. Salmeron Sanchez, and M. M. Stevens, Assembling living building blocks to engineer complex tissues, Adv. Funct. Mater. **30**, 1909009 (2020).
[15] U. A. Gurkan, S. Tasoglu, D. Kavaz, M. C. Demirel, and U. Demirci, Emerging technologies for assembly of microscale hydrogels, Adv. Healthcare Mater. **1**, 149 (2012).
[16] D. Baresch and V. Garbin, Acoustic trapping of microbubbles in complex environments and controlled payload release, Proc. Natl. Acad. Sci. U.S.A. **117**, 15490 (2020).
[17] Z. Ma, K. Melde, A. G. Athanassiadis, M. Schau, H. Richter, T. Qiu, and P. Fischer, Spatial ultrasound modulation by digitally controlling microbubble arrays, Nat. Commun. **11**, 4537 (2020).
[18] Z. Ma, A. W. Holle, K. Melde, T. Qiu, K. Poeppel, V. M. Kadiri, and P. Fischer, Acoustic holographic cell patterning in a biocompatible hydrogel, Adv. Mater. **32**, 1904181 (2020).
[19] A. Marzo, S. A. Seah, B. W. Drinkwater, D. R. Sahoo, B. Long, and S. Subramanian, Holographic acoustic elements for manipulation of levitated objects, Nat. Commun. **6**, 8661 (2015).
[20] K. Melde, A. G. Mark, T. Qiu, and P. Fischer, Holograms for acoustics, Nature (London) **537**, 518 (2016).
[21] M. Caleap and B. W. Drinkwater, Acoustically trapped colloidal crystals that are reconfigurable in real time, Proc. Natl. Acad. Sci. U.S.A. **111**, 6226 (2014).
[22] C. E. Owens, C. W. Shields, D. F. Cruz, P. Charbonneau, and G. P. López, Highly parallel acoustic assembly of microparticles into well-ordered colloidal crystallites, Soft Matter **12**, 717 (2016).
[23] S. Li, F. Guo, Y. Chen, X. Ding, P. Li, L. Wang, C. E. Cameron, and T. J. Huang, Standing surface acoustic wave based cell coculture, Anal. Chem. **86**, 9853 (2014).
[24] P. Chen, S. Güven, O. B. Usta, M. L. Yarmush, and U. Demirci, Biotunable acoustic node assembly of organoids, Adv. Healthcare Mater. **4**, 1937 (2015).
[25] H. Bruus, Acoustofluidics 7: The acoustic radiation force on small particles, Lab Chip **12**, 1014 (2012).
[26] P. B. Muller, R. Barnkob, M. J. H. Jensen, and H. Bruus, A numerical study of microparticle acoustophoresis driven by acoustic radiation forces and streaming-induced drag forces, Lab Chip **12**, 4617 (2012).
[27] T. Qiu, S. Palagi, A. G. Mark, K. Melde, F. Adams, and P. Fischer, Wireless actuation with functional acoustic surfaces, Appl. Phys. Lett. **109**, 191602 (2016).
[28] T. Qiu, F. Adams, S. Palagi, K. Melde, A. Mark, U. Wetterauer, A. Miernik, and P. Fischer, Wireless acoustic-surface actuators for miniaturized endoscopes, ACS Appl. Mater. Interfaces **9**, 42536 (2017).
[29] X. Guo, Z. Ma, R. Goyal, M. Jeong, W. Pang, P. Fischer, X. Duan, and T. Qiu, Acoustofluidic tweezers for the 3D manipulation of microparticles, in *2020 IEEE International Conference on Robotics and Automation (ICRA)* (IEEE, Paris, 2020), pp. 11392–11397, 10.1109/ICRA40945.2020.9197265.
[30] V. Bjerknes, *Fields of Force*, Publication of the Ernest Kempton Adams Fund for Physical Research (Columbia University Press, New York, 1906).
[31] D. Rabaud, P. Thibault, M. Mathieu, and P. Marmottant, Acoustically Bound Microfluidic Bubble Crystals, Phys. Rev. Lett. **106**, 134501 (2011).
[32] D. Rabaud, P. Thibault, J.-P. Raven, O. Hugon, E. Lacot, and P. Marmottant, Manipulation of confined bubbles in a thin microchannel: Drag and acoustic Bjerknes forces, Phys. Fluids **23**, 042003 (2011).
[33] G. Regnault, C. Mauger, P. Blanc-Benon, and C. Inserra, Secondary radiation force between two closely spaced acoustic bubbles, Phys. Rev. E **102**, 031101(R) (2020).
[34] M. Lanoy, C. Derec, A. Tourin, and V. Leroy, Manipulating bubbles with secondary Bjerknes forces, Appl. Phys. Lett. **107**, 214101 (2015).
[35] J. G. S. Moo, C. C. Mayorga-Martinez, H. Wang, W. Z. Teo, B. H. Tan, T. D. Luong, S. R. Gonzalez-Avila, C.-D. Ohl, and M. Pumera, Bjerknes forces in motion: Long-range translational motion and chiral directionality switching in bubble-propelled micromotors via an ultrasonic pathway, Adv. Funct. Mater. **28**, 1702618 (2018).
[36] L. A. Crum, Bjerknes forces on bubbles in a stationary sound field, J. Acoust. Soc. Am. **57**, 1363 (1975).
[37] See Supplemental Material at http://link.aps.org/supplemental/10.1103/PhysRevLett.128.254502 for details of calculations and experimental parameters, which includes Refs. [38–48].
[38] N. W. Ashcroft, N. D. Mermin *et al.*, *Solid State Physics* (Holt, Rinehart and Winston, New York, 1976).
[39] C. Chindam, N. Nama, M. Ian Lapsley, F. Costanzo, and T. Jun Huang, Theory and experiment on resonant frequencies of liquid-air interfaces trapped in microfluidic devices, J. Appl. Phys. **114**, 194503 (2013).
[40] D. J. Griffiths, Dipoles at rest, Am. J. Phys. **60**, 979 (1992).
[41] D. J. Griffiths, *Introduction to Electrodynamics* (Prentice Hall of India, New Delhi, 2013).
[42] D. Gritsenko, Y. Lin, V. Hovorka, Z. Zhang, A. Ahmadianyazdi, and J. Xu, Vibrational modes prediction for water-air bubbles trapped in circular microcavities, Phys. Fluids **30**, 082001 (2018).

[43] C. Kittel, *Introduction to Solid State Physics* (John Wiley and Sons, New York, 1976).
[44] T. G. Leighton, *The Acoustic Bubble* (Elsevier, New York, 1994).
[45] V. Leroy, M. Devaud, T. Hocquet, and J. C. Bacri, The bubble cloud as an N-degree of freedom harmonic oscillator, Eur. Phys. J. E **17**, 189 (2005).
[46] E. Lifshitz and L. Landau, *Course of Theoretical Physics: Fluid Mechanics* (Butterworth-Heinemann, Oxford, England, 1987).
[47] A. Mata, A. J. Fleischman, and S. Roy, Characterization of polydimethylsiloxane (PDMS) properties for biomedical micro/nanosystems, Biomed. Microdevices **7**, 281 (2005).
[48] F. L. Pedrotti, L. M. Pedrotti, and L. S. Pedrotti, *Introduction to Optics* (Cambridge University Press, Cambridge, 2017).
[49] D. Qin, Y. Xia, and G. M. Whitesides, Soft lithography for micro- and nanoscale patterning, Nat. Protocols **5**, 491 (2010).